AGU PUBLICATIONS

Geophysical Research Letters

RESEARCH LETTER
10.1002/2017GL076110

Key Points:
- Refined fault geometries using precise aftershock relocation and updated coseismic and aseismic slips for the Emilia main shocks
- Aftershock decay rate deviates from classical Omori-like pattern and *Vp/Vs* changes along the fault system during the sequence
- Fluid pressure pulse drove the seismic sequence and triggered the second main shock

Supporting Information:
- Supporting Information S1

Correspondence to:
G. Pezzo,
giuseppe.pezzo@ingv.it

Citation:
Pezzo, G., De Gori, P., Lucente, F. P., & Chiarabba, C. (2018). Pore pressure pulse drove the 2012 Emilia (Italy) series of earthquakes. *Geophysical Research Letters*, *45*, 682–690. https://doi.org/10.1002/2017GL076110

Received 27 JUL 2017
Accepted 1 JAN 2018
Accepted article online 8 JAN 2018
Published online 24 JAN 2018

Pore Pressure Pulse Drove the 2012 Emilia (Italy) Series of Earthquakes

Giuseppe Pezzo[1], Pasquale De Gori[1], Francesco Pio Lucente[1], and Claudio Chiarabba[1]

[1]Istituto Nazionale di Geofisica e Vulcanologia, Rome, Italy

Abstract The 2012 Emilia earthquakes sequence is the first debated case in Italy of destructive event possibly induced by anthropic activity. During this sequence, two main earthquakes occurred separated by 9 days on contiguous thrust faults. Scientific commissions engaged by the Italian government reported complementary scenarios on the potential trigger mechanism ascribable to exploitation of a nearby oil field. In this study, we combine a refined geodetic source model constrained by precise aftershock locations and an improved tomographic model of the area to define the geometrical relation between the activated faults and investigate possible triggering mechanisms. An aftershock decay rate that deviates from the classical Omori-like pattern and *Vp/Vs* changes along the fault system suggests that natural pore pressure pulse drove the space-time evolution of seismicity and the activation of the second main shock.

Plain Language Summary Induced seismicity has increasingly become a major topic among Earth scientists. Concerns about a causative role played by the oil-gas extraction and/or the deep injection of disposable water in triggering earthquakes have grown fast in recent years, with many implications for public regulators and stakeholders. We present and discuss the 2012 Emilia (Italy) earthquakes sequence, which is the first debated case in Italy of destructive events possibly induced by anthropic activity. We use coseismic ground deformation measurements and seismic data to define the geometrical relation between the activated faults and investigate possible triggering mechanisms. Our results indicate that fluid pressure at the base of the system was responsible for triggering the two 2012 main earthquakes and exclude any anthropic trigger. Thus, cautious monitoring of seismicity, deformation, and pore pressure can recognize active processes along active faults that can potentially cause earthquakes. Such monitoring should be mandatory to conjugate exploitation activity in seismic active areas with safeness and sustainability.

1. Introduction

On 20 and 29 May 2012, two shocks (M_w 6.0 and M_w 5.8) struck the Emilia region in northern Italy (Govoni et al., 2014), causing 28 victims and an economic loss of about 14 billion Euro, revealing once more how challenging the management of seismic risk is in intensely urbanized and highly productive areas. The possibility that anthropic activity favored the earthquake occurrence rapidly created concerns in the population and controversies for private and public stakeholders, which caused the temporary suspension of oil and gas activities. Thus, the 2012 earthquakes are the first modern-time sequence in Italy that led a wide community to face the problem of induced seismicity.

Earthquakes occurred in a relatively slowly deforming region, where the few mm/yr of compressional rate is accommodated by the Apennines frontal thrust (Bennett et al., 2012). Seismicity spreads on a multibranched system of fault segments, whose envelope forms an arc-like thrust front buried beneath the Po plain (Figures 1a and 1b).

Coseismic slip developed on two patches of the parallel offset and blind Ferrara and Mirandola thrust faults (Figure 1c) (Bonini et al., 2014; Chiarabba et al., 2014; Pezzo et al., 2013), uplifting a Mesozoic carbonate multilayer (Figure 1b). The Mirandola anticline, site of oil exploitation, is the bulge of this imbricated and buried fault-and-fold system (Figures 1a and 1b). The Mirandola thrust slipped at 0.86 ± 0.38 mm/yr during the last 0.4 Myr (Maesano et al., 2015) and the anticline experienced an uplift of about 0.2 mm/yr during the past 0.1 kyr (Scrocca et al., 2007), while the net vertical balance of the area is negative for the large regional subsidence. Vertical slip during the 2012 earthquakes is consistent with the growth rate of the anticline, suggesting that the process remained stationary during the entire Holocene (Pezzo et al., 2013). Since the small deformation rate, recurrence time between large earthquakes is on the order of thousand years (Rovida

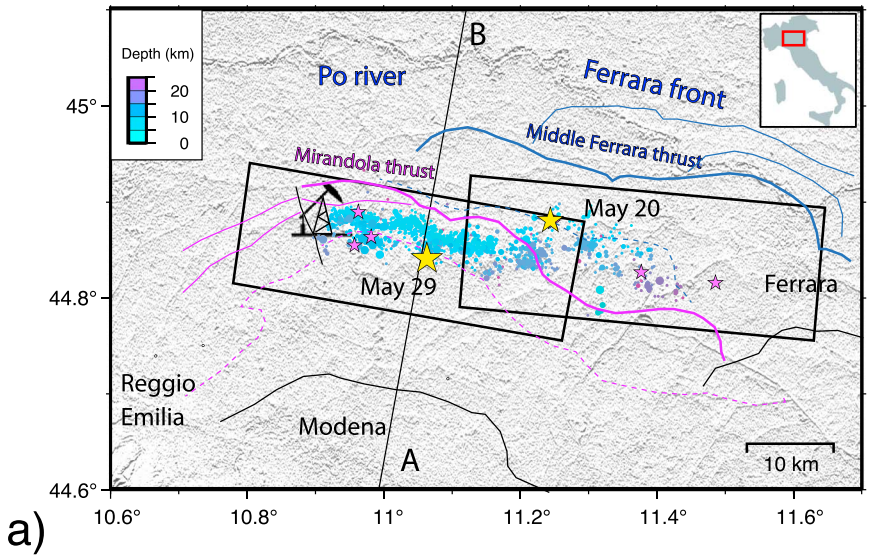

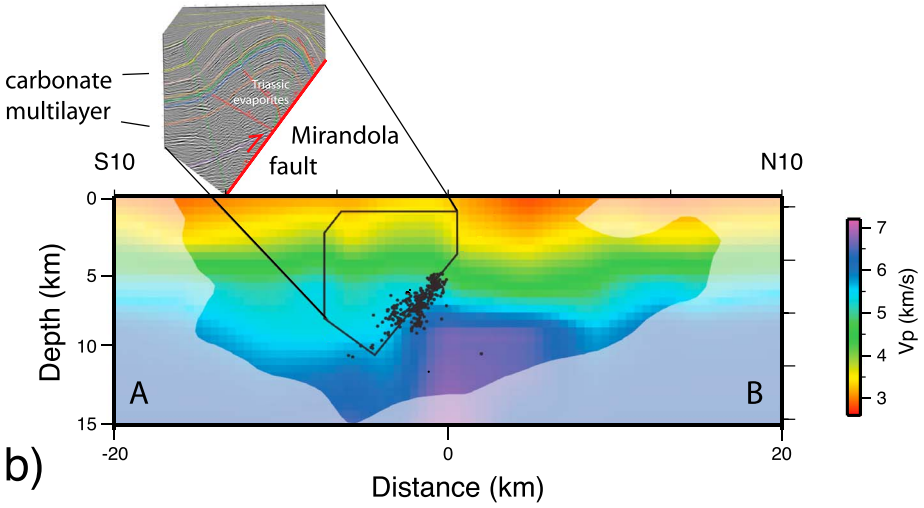

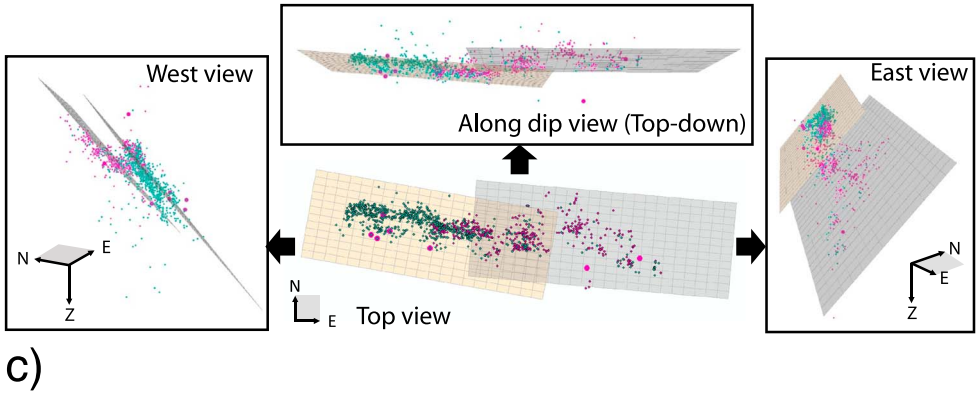

Figure 1. The 2012 Emilia earthquakes fault system. (a) Map showing the 2012 Emilia seismic sequence together with the main tectonic structures, namely, the Ferrara and Mirandola thrust fronts. The black boxes are the surface projections of the modeled south dipping Ferrara and Mirandola faults, constrained by the aftershock relocations. Earthquakes are sized by magnitude and color-coded by depth according to the scale on the top-left inset. The larger yellow stars are the two main shocks (M_W 6.0 and M_W 5.8); the smaller purple stars are the largest aftershocks ($M_L \geq 5.0$). (b) Tomographic section (A-B trace in Figure 1a) across the Mirandola fold and thrust structures showing *P* wave velocities together with the aftershock relocations. Figure 1b also shows a portion of the seismic section highlighting the Mesozoic carbonatic core of the Mirandola anticline. (c) Top, east, west, and along dip views of the modeled Ferrara (gray) and Mirandola (beige) faults. The 3-D views show as the modeled fault planes fit the 2012 hypocenters occurred before (purple) and after (green) the 29 May earthquake.

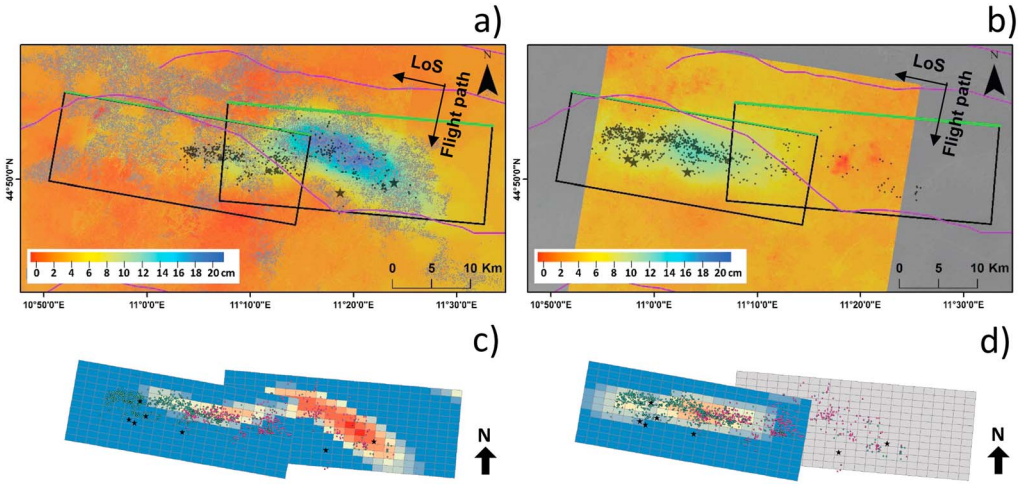

Figure 2. Coseismic displacements. Maps of the (a) 20 and (b) 29 May earthquakes computed by Pezzo et al. (2013), used for the new inversion. Displacements are in line of sight (LoS): positive values (blue) are approaching the sensor, and vice versa for the negative ones (red). The black boxes represent the surface projections of the modeled faults, and the green lines are the upper tips. Seismicity (the stars are $M_w \geq 5.0$) that occurred during the two time periods is also reported; the purple lines represent the surface projections of the main buried thrusts. Coseismic slip distribution of the (c) 20 and (d) 29 May shocks, respectively, obtained by inverting InSAR and GPS data. Note in Figure 2c the aseismic slip patches on the eastern border of the Mirandola fault corresponding to the whisker-shaped ground deformation observable close to the main lobe in Figure 2a.

et al., 2011). In such cases, transient changes in local stress, like those potentially related to anthropic activity (McGarr et al., 2002), may have effects on the timing of failure (Ellsworth, 2013). In this study, we reanalyzed the sequence trying to make inference on the triggering mechanisms that promoted the additional activation of the Mirandola fault after the first 20 May main shock.

2. Geometry of the Faults

Different interpretations of seismic profiles lead to contrasting fault models and ambiguity on the hydraulic connectivity between faults and the oil reservoir (Astiz et al., 2014; Styles et al., 2014). Previously, seismic source models based on geodetic data proposed planar (Bignami et al., 2012; Serpelloni et al., 2012) or listric faults (Cheloni et al., 2016; Pezzo et al., 2013; Tizzani et al., 2013) for the 2012 events.

In this work we use the Pezzo et al. (2013) model, updating geometric parameters using accurate aftershock locations, recomputed in this study with the new 3-D model, to obtain two planar faults corresponding to the Middle Ferrara (east) and the Mirandola (west) thrusts (Figure 1c). Slips are updated reinverting coseismic SAR (Figures 2a and 2b) and GPS ground displacements as shown by Pezzo et al. (2013), obtaining consistent slip distributions. Refined parameters for 20 May (middle Ferrara thrust) and 29 May (Mirandola thrust) sources are respectively as follows: length: 34.5 and 31.5 km; width 19.5 and 18 km; top depth 1 km, strike 95°, and 100°; dip 50°; rake 70° and 90°; and maximum slip 110 and 56 cm.

Hypocenters follow the slipping fault patches, and a transient aseismic slip along the second shock plane corresponds to a secondary whisker-shaped ground deformation close to the main coseismic deformation lobe of the first shock (Figures 2a and 2c; see also Pezzo et al., 2013). In the period between the two shocks, seismicity jumps from the Ferrara to the Mirandola fault and no major seismic events are localized where the aseismic slip occurred. Seismicity after the second 29 May main shock aligned along the south-dipping Mirandola thrust, for an extent of 15 km.

3. Aftershock Decay

Aftershock rates that do not follow an Omori-like decay can be evidence for high fluid pressure (Lombardi et al., 2010; Nur & Booker, 1972) or stressing on faults (Toda et al., 2002). To address whether transient effects sustained the sequence, we compute the decay rate by considering time interval of progressively increasing

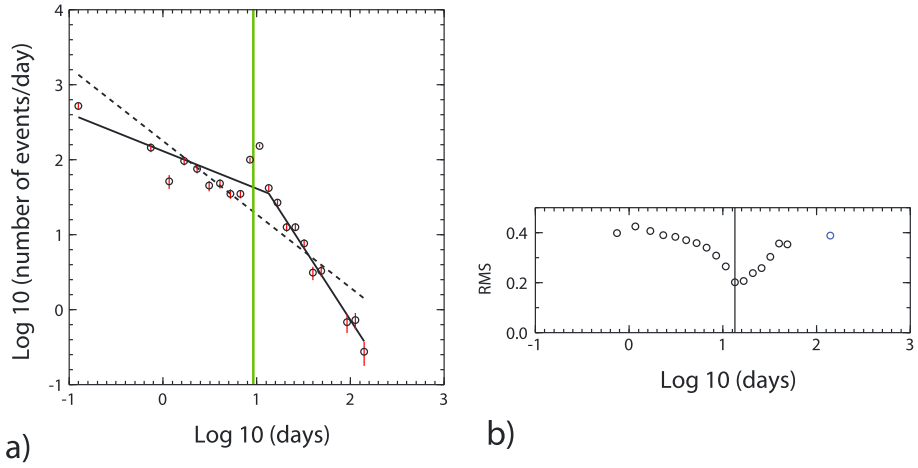

Figure 3. Aftershock decay rate. (a) Number of aftershocks/day as a function of the time elapsed from the 20 May main shock for a 2.2 completeness magnitude threshold. The green vertical bar represents the time of occurrence of the second main shock. The red vertical bars on each point represent uncertainties of the computed rates. The dashed black line represents a single-slope Omori-like decay. The continuous black line represents a two-line decay model where the first part was forced to be diffusion-like (see text for details). (b) Misfit functions for the two-line fit. The vertical bar through panels indicates the time of the minimum misfit, at the intersection of the two continuous line segments in Figure 3a.

duration from 6 h to about 29 days. The duration of the first interval has been chosen after a thorough completeness analysis of the seismic catalog (M_L 2.2 from 6 h after the shock onward). Uncertainties on the rates were calculated by bootstrapping the data sets with 100 realizations. We fit the aftershocks/day rates with (a) a single-slope Omori-figure like model (dashed line in Figure 3a) and (b) a two-line decay model (continuous line in Figure 3b), where the first part was forced to be diffusion-like (power law exponent of the Omori law $p \approx 0.5$), whereas the slope of the second part and its intersection with the first one were free to vary (Malagnini et al., 2012). The corrected Akaike criterion indicates that, with 99% likelihood, the two-slope model fits the aftershock decay rate significantly better, in a statistical sense, than a single-slope Omori model. The change in the decay rate occurs on the time of second main shock (vertical bar in Figure 3b).

The slope of the aftershock decay during the period preceding the second main shock is flatter (power law exponent of the Omori law $p \approx 0.5$) than that predicted by the Omori law (power law exponent of the Omori law $p \approx 1$), and the rate has decay consistent with high fluid pressure or stressing on the fault system.

4. Tomographic Models

To look for transient processes, we compute *Vp*/*Vs* models of the fault system by using standard inversion techniques (Eberhart-Phillips & Reyners, 1997) and a huge set of *P* and *S* wave arrival time data collected at a dense temporary network (Chiarabba et al., 2014) and at the Cavone oil field network. We use the 1-D *Vp* starting model of Chiarabba et al. (2014); starting *Vp*/*Vs* has been chosen according to the computed Wadati (1933) diagram, as detailed in the supporting information (Eberhart-Phillips & Michael, 1998; Haslinger, 1998; Thurber, 1983; Toomey & Foulger, 1989).

Time lapse imaging is computed for the entire period (20 May to 30 June) and for the two epochs before and after the second main shock (Epoch A: 20–29 May and Epoch B: 29 May to 30 June) following either a direct approach or that proposed by Foulger et al. (2003) and Patanè et al. (2006).

The inversion of the entire data set, which consists of 23,270 P and 15,654 S-P arrival times at 49 stations from 1,799 earthquakes, has final RMS of 0.24 s, with a variance improvement equal to 75%. The inversion for the first epoch subset (Epoch A), which consists of 8,734 P and 5,835 S-P arrival times at 49 stations from 752 earthquakes, has final RMS of 0.23 s, with a variance improvement equal to 71%. The inversion for the second epoch subset (Epoch B) consists of 14,536 and 9,819 P and S-P arrival times at 48 stations from 1,054 earthquakes and has final RMS of 0.24 s, with a variance improvement equal to 78% (a full description of the tomographic inversion results is reported in Figures S1–S4 in the supporting information).

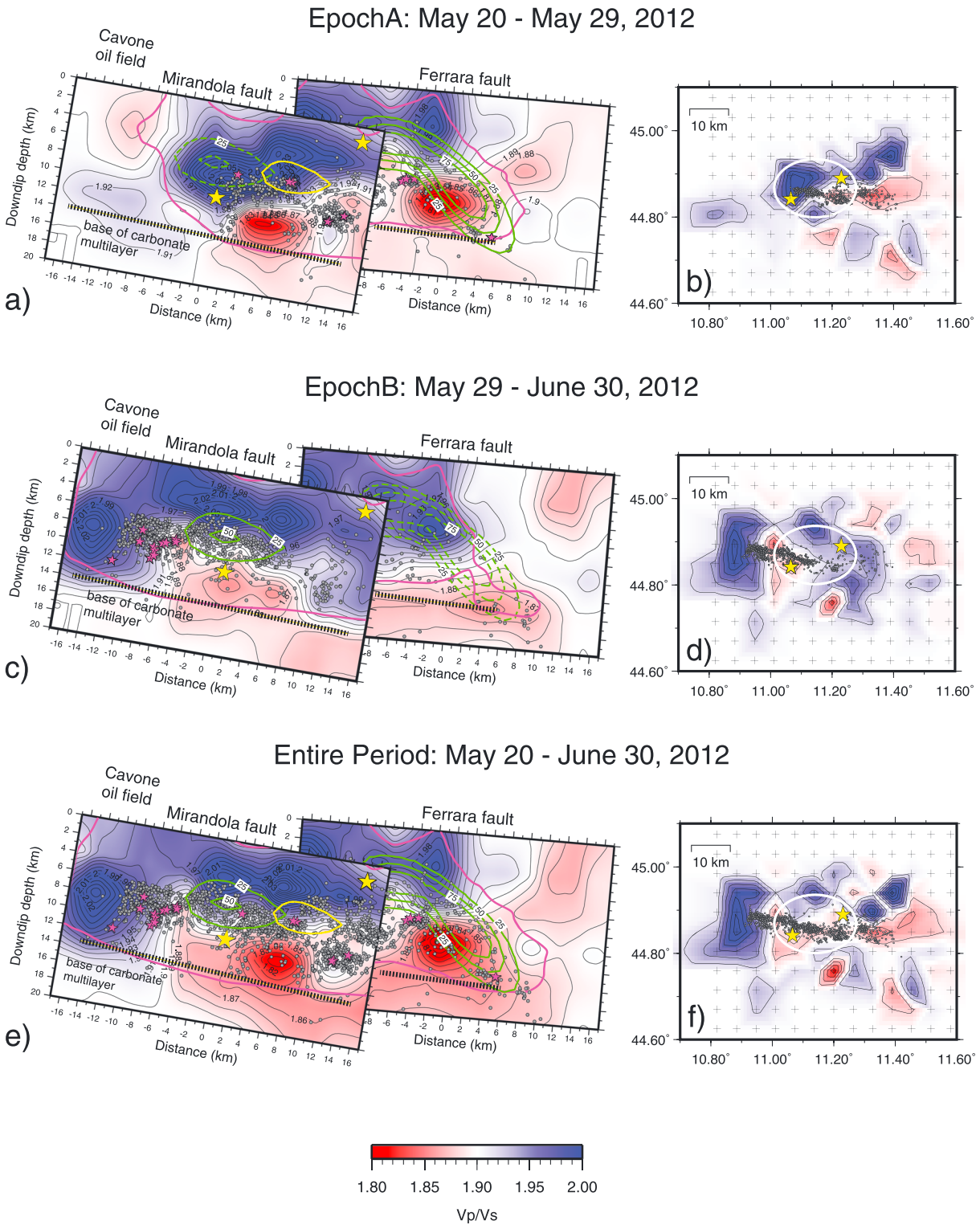

Figure 4. *Vp/Vs* models. (a–f) *Vp/Vs* distribution along the Ferrara and Mirandola thrust fault system in downdip view (Figures 4a, 4c, and 4e) and in map view at seismogenic depth (Figures 4b, 4d, and 4f) for the Epoch A (20–29 May), the Epoch B (29 May to 30 June), and the entire period (20 May to 30 June), respectively. Coseismic slips of the two main shocks (green contour, dashed outside the associated epoch) and of the aseismic slip (yellow contour) are shown with aftershocks that occurred during the three distinct epochs (gray circles). Slip contours are from the ground displacement inversion (Figure 2). The two main shock hypocenters (yellow stars) are shown, along with the $M_L \geq 4.0$ earthquakes (purple stars) occurring in each epoch in the map view (Figures 4b, 4d, and 4f); the gray circles are the aftershocks that occurred during the three distinct epochs in the depth range 6–9 km. Nodes in the inverted models are also shown (crosses). The white elliptical line highlights the volume of rock between the two main shock hypocenters, where the larger changes in the *Vp/Vs* ratio are found through the epochs.

In the second approach, designed to mitigate artifacts caused by difference of data coverage, the entire period model is used as the starting model for the inversion of subepochs. We obtain final RMSs of 0.22 s and 0.24 s and variance improvements of 30% and 36%, for the inversion of Epoch A and Epoch B, respectively. The full description of the results obtained for Epoch A is shown in Figure S5.

Time-consistent resolution for the inversions has been verified with full resolution analysis and several synthetic tests, reported in Figures S2, S4, and S6–S9. We also verified the performance of the two approaches in time-lapse imaging with specific test (see Figures S10–S12).

5. *Vp*/*Vs* Changes Before the Second Main Shock (20–29 May)

The distribution of the *Vp*/*Vs* ratio varies consistently along the fault system before and after the second shock, especially in the rock volume between the two main shock hypocenters (Figure 4). The interpretation of the subsurface geological model is in accordance with Chiarabba et al. (2014) and constrained by seismic profiles (Astiz et al., 2014).

Many different factors can contribute to change the elastic properties of rocks—thus their seismic velocity, such as temperature, pressure, fracturing, and fluid saturation. After an earthquake struck, sudden changes of these physical quantities may cause short-term variation of seismic velocities. However, the *Vp*/*Vs* ratio appears to be more sensitive to the presence of fluid but less sensitive to changes in temperature and pressure (Christensen, 1996). This, along with the aftershock decay rate observed before the second main shock (Figure 3), led us to interpret the large *Vp*/*Vs* changes observed (Figure 4) in terms of fluid saturation and diffusion processes.

We focus on three main features:

1. High *Vp*/*Vs* anomaly on the Mirandola fault (Figure 4a), in the volume where aseismic deformation occurred and in the segment where the seismicity jumped after the first main shock (eastern yellow star in Figures 4a–4f). This anomaly could be generated by pressurized fluids within the water-saturated carbonate multilayer, with lowering of shear wave velocity because cracks are forced to remain opened (O'Connell & Budiansky, 1974). The high *Vp*/*Vs* pressurized volume is well evident in the Epoch A, that is, in the 9 days before the second main shock (western yellow star in Figures 4a–4f) between the two hypocenters (Figures 4a and 4b), while a decrease of *Vp*/*Vs* and of fluid pressure after the second event (Epoch B) is observed along the ruptured fault (Figures 4c and 4d).
2. Expanding low *Vp*/*Vs* anomalies at the base of the carbonate multilayer from Epoch A to Epoch B (Figures 4a, 4c, and 4e). We interpret the low *Vp*/*Vs* anomaly as generated by fluid depressurization within the Triassic evaporitic layer after the main shocks (Mavko & Vanorio, 2010; Nur, 1972; O'Connell & Budiansky, 1974).
3. Coincidence between high *Vp*/*Vs*, that is, high fluid pressure, coseismic, and aseismic slip before (Figure 4a), and seismicity after, the second shock on the Mirandola fault (Figure 4c).

Vp/*Vs* changes before the second main shock are highlighted by the difference between Epoch A and the entire period, computed following the second approach. High *Vp*/*Vs* anomaly along the slip patch of the Mirandola fault (Figure 5a) and close to the two main shock hypocenters (Figure 5b) along with clustering of aftershocks on the slipped fault patches (Figure 5a) suggest deep fluids repressurized of the fault.

6. Discussion

According to the small tectonic rate and the long time passed since the last event (>700 years), a significant amount of slip was accumulated on the Ferrara thrust front, which was reasonably not far to rupture. Either anthropic or natural processes might have altered this low-rate tectonic loading, triggering the events.

Aftershock rate suggests that a transient effect was superposed to the normal decay that is consistent with fluid overpressure along the fault system, well defined by high *Vp*/*Vs* anomalies (Figures 4a and 4b and 5). A suprahydrostatic regime acting on the 29 May rupture plane, which could have promoted the activation of the thrust fault, is also inferred by Volpe and Piersanti (2016).

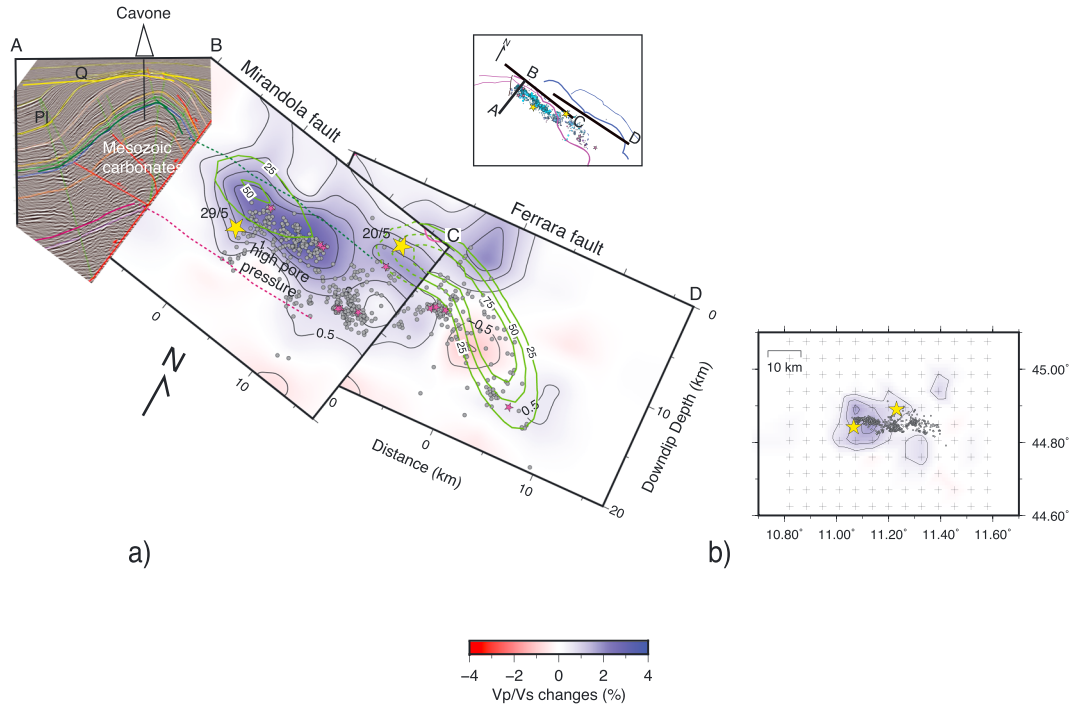

Figure 5. *Vp/Vs* differences. (a) Downdip view of the *Vp/Vs* difference between the Epoch A (20–29 May) model inverted from the 3-D starting model (see text for details) and the entire period, plotted on the contiguous Ferrara and Mirandola thrust faults (see the top panel for geometry at surface). The inset panel on the left shows a seismic profile across the Mirandola fault (modified from the Cavone report). Earthquakes on the downdip sections are those occurred in the Epoch A. The symbols not expressly indicated are the same as those in Figure 4. The continuity of the main horizons independently extracted by tomography and seismic modeling are evidenced on the top view of the fault. The high *Vp/Vs* transient anomaly, which we interpret as a pressurized patch on the Mirandola fault, extends from the area between the two main shock hypocenters (yellow stars) to that of high coseismic slip on the Mirandola fault. Note that the high-pressure region on the Mirandola fault is in continuity with that of the Ferrara fault ruptured during the first main shock. (b) Map view of the *Vp/Vs* difference at seismogenic depth. The symbols are the same as those in previous figures/panels.

In the assumption that transient *Vp/Vs* changes are related to fluid pressure variation, the observed high *Vp/Vs* in Epoch A (Figures 4a and 4b) with a positive anomaly at least 4% higher (Figure 5) qualitatively suggests a pressure increase in the order of several MPa (Dvorkin et al., 1999; Trippetta et al., 2010; Wang, 1997).

The pressure change seems much higher than both the static stress load on the fault (0.4 and 0.6 MPa, calculated by Nespoli et al. (2017) and Pezzo et al. (2013), respectively); the poroelastic stress change (Albano et al., 2017) and the stress changes generated by depletion of the reservoir or fluid reinjection at the Cavone disposing well, which are in the order of a few bars (Juanes et al., 2016). Consistent with our interpretation, model of depletion-induced stress shows a negligible trigger potential at the hypocenters of the two main shocks (Dahm et al., 2015).

In our interpretation, high-amplitude pressure pulse (Koerner et al., 2004) propagated through a highly permeable fracture system generated after the first shock and confined in the Mesozoic carbonate layer (Figure 5a). The high pore pressure pulse at the base of the carbonate multilayer (Figures 4a and 5a) first induced the aseismic slip on the Mirandola fault and then triggered the second main shock. This is the first observational evidence for a triggering mechanism similar to that proposed for the 1997 Colfiorito earthquakes (Miller et al., 2004). The rupturing of relatively high angle thrust faults, interpreted as inverted normal faults (Chiarabba et al., 2014), is favored by high fluid pressure pulse, as observed by Sibson (2009). Our results sustain that fault reactivation and multiple main shock sequences, which seem to be common to other seismogenic structures in the Apennines (Malagnini et al., 2012, and references therein), may be driven by fluid overpressure pulse at the base of the fault system. Following our interpretation, stress changes caused by Cavone field exploitation are poorly significant in the triggering of the second main

shock. Dense seismic networks and sophisticated analyses, like those recently suggested by the Ministry for the Economic Development, are necessary to address the potential of anthropic activity to trigger large destructive earthquake.

Acknowledgments
We thank funding from the Ministero dello Sviluppo Economico. We also thank S. Atzori, E. Serpelloni, and S. Salvi for supporting in SAR-GPS data inversion and A. Marchetti for help with local earthquake data. The data used are listed in the references and supporting information.

References

Albano, M., Barba, S., Solaro, G., Pepe, A., Bignami, C., Moro, M., … Stramondo, S. (2017). Aftershocks, groundwater changes and postseismic ground displacements related to pore pressure gradients: Insights from the 2012 Emilia-Romagna earthquake. *Journal of Geophysical Research: Solid Earth*, *122*, 5622–5638. https://doi.org/10.1002/2017JB014009

Astiz, L., Dieterich, J. H., Frohlich, C., Hager, B. H., Juanes, R., & Shaw, J. H. (2014). On the potential for induced seismicity at the Cavone oilfield: Analysis of geological and geophysical data, and geomechanical modeling, Report for the Laboratorio di Monitoraggio Cavone (139 pp.). Retrieved from http://labcavone.it/documenti/32/allegatrapporto-studiogiacimento.pdf

Bennett, R. A., Serpelloni, E., Hreinsdóttir, S., Brandon, M. T., Buble, G., Basic, T., … Montanari, A. (2012). Syn-convergent extension observed using the RETREAT GPS network, northern Apennines Italy. *Journal of Geophysical Research*, *117*, B04408. https://doi.org/10.1029/2011JB008744

Bignami, C., Burrato, P., Cannelli, V., Chini, M., Falcucci, E., Ferretti, A., … Vannoli, P. (2012). Coseismic deformation pattern of the Emilia 2012 seismic sequence imaged by Radarsat-1 interferometry. *Annals of Geophysics*, *55*(4), 789–793. https://doi.org/10.4401/ag-6157

Bonini, L., Toscani, G., & Seno, S. (2014). Three-dimensional segmentation and different rupture behavior during the 2012 Emilia seismic sequence (northern Italy). *Tectonophysics*, *630*, 33–42. https://doi.org/10.1016/j.tecto.2014.95.006

Cheloni, D., Giuliani, R., D'Agostino, N., Mattone, M., Bonano, M., Fornaro, G., … Atzori, S. (2016). New insights into fault activation and stress transfer between en echelon thrusts: The 2012 Emilia, northern Italy, earthquake sequence. *Journal of Geophysical Research: Solid Earth*, *121*, 4742–4766. https://doi.org/10.1002/2016JB012823

Chiarabba, C., De Gori, P., Improta, L., Lucente, F. P., Moretti, M., Govoni, A., … Nardi, A. (2014). Frontal compression along the Apennines thrust system: The Emilia 2012 example from seismicity to crustal structure. *Journal of Geodynamics*, *82*, 98–109. https://doi.org/10.1016/j.jog.2014.09.003

Christensen, N. I. (1996). Poisson's ratio and crustal seismology. *Journal of Geophysical Research*, *101*, 3139–3156. https://doi.org/10.1029/95JB03446

Dahm, T., Cesca, S., Hainzl, S., Braun, T., & Krüger, F. (2015). Discrimination between induced, triggered, and natural earthquakes close to hydrocarbon reservoirs: A probabilistic approach based on the modeling of depletion-induced stress changes and seismological source parameters. *Journal of Geophysical Research: Solid Earth*, *120*, 2491–2509. https://doi.org/10.1002/2014JB011778

Dvorkin, J., Mavko, G., & Nur, A. (1999). Overpressure detection from compressional- and shear- wave data. *Geophysical Research Letters*, *26*, 3417–3420. https://doi.org/10.1029/1999GL008382

Eberhart-Phillips, D., & Michael, A. J. (1998). Seismotectonics of the Loma Prieta, California, region determined from three-dimensional V P, V P/V S, and seismicity. *Journal of Geophysical Research*, *103*, 21,099–21,120. https://doi.org/10.1029/98JB01984

Eberhart-Phillips, D., & Reyners, M. (1997). Continental subduction and three-dimensional crustal structure: The northern South Island, New Zealand. *Journal of Geophysical Research*, *102*, 11,843–11,861. https://doi.org/10.1029/96JB03555

Ellsworth, W. L. (2013). Injection-induced earthquakes. *Science*, *341*(6142), 1225942. https://doi.org/10.1126/science.1225942

Foulger, G. R., Julian, B. R., Pitt, A. M., Hill, D. P., Malin, P. E., & Shalev, E. (2003). Three-dimensional crustal structure of Long Valley caldera, California, and evidence for the migration of CO_2 under Mammoth Mountain. *Journal of Geophysical Research*, *108*(B3), 2147. https://doi.org/10.1029/2000JB000041

Govoni, A., Marchetti, A., de Gori, P., di Bona, M., Lucente, F. P., Improta, L., … Piccinini, D. (2014). The 2012 Emilia seismic sequence (northern Italy): Imaging the thrust fault system by accurate aftershock location. *Tectonophysics*, *622*, 44–55. https://doi.org/10.1016/j.tecto.2014.02.013

Haslinger, F. (1998). Velocity structure, seismicity and seismotectonics of northwestern Greece between the Gulf of Arta and Zakynthos, (PhD thesis). Dep. Geophys., ETH, Zurich, Switzerland.

Juanes, R., Jha, B., Hager, B. H., Shaw, J. H., Plesch, A., Astiz, L., … Frohlich, C. (2016). Were the May 2012 Emilia-Romagna earthquakes induced? A coupled flow-geomechanics modeling assessment. *Geophysical Research Letters*, *43*, 6891–6897. https://doi.org/10.1002/2016GL069284

Koerner, A., Kissling, E., & Miller, S. A. (2004). A model of deep crustal fluid flow following the M_w = 8.0 Antofagasta, Chile, earthquake. *Journal of Geophysical Research*, *109*, B06307. https://doi.org/10.1029/2003JB002816

Lombardi, A. M., Marzocchi, W., & Cocco, M. (2010). On the increase of background seismicity rate during the 1997–1998 Umbria-Marche, Central Italy, sequence: Apparent variation or fluid-driven triggering? *Bulletin of the Seismological Society of America*, *100*(3), 1138–1152. https://doi.org/10.1785/0120090077

Maesano, F. E., D'Ambrogi, C., Burrato, P., & Toscani, G. (2015). Slip-rates of blind thrusts in slow deforming areas: Examples from the Po Plain (Italy). *Tectonophysics*, *643*, 8–25. https://doi.org/10.1016/j.tecto.2014.12.007

Malagnini, L., Lucente, F. P., Gori, P. D., Akinci, A., & Munafo, I. (2012). Control of pore fluid pressure diffusion on fault failure mode: Insights from the 2009 L'Aquila seismic sequence. *Journal of Geophysical Research*, *117*, B05302. https://doi.org/10.1029/2011JB008911

Mavko, G., & Vanorio, T. (2010). The influence of pore fluids and frequency on apparent effective stress behavior of seismic velocities. *Geophysics*, *75*(1), N1–N7. https://doi.org/10.1190/1.3277251

McGarr, A., Simpson, D., & Seeber, L. (2002). 40 case histories of induced and triggered seismicity. *International Geophysics*, *81*, 647–661. https://doi.org/10.1016/S0074-6142(02)80243-1

Miller, S. A., Collettini, C., Chiaraluce, L., Cocco, M., Barchi, M., & Kaus, J. P. (2004). Aftershocks driven by a high-pressure CO_2 source at depth. *Nature*, *427*(6976), 724–727. https://doi.org/10.1038/nature02251

Nespoli, M., Belardinelli, M. E., Anderlini, L., Bonafede, M., Pezzo, G., Todesco, M., & Rinaldi, A. P. (2017). Effects of layered crust on the coseismic slip inversion and related CFF variations: Hints from the 2012 Emilia Romagna earthquake. *Physics of the Earth and Planetary Interiors*, *273*, 23–35. https://doi.org/10.1016/j.pepi.2017.10.011

Nur, A. (1972). Dilatancy, pore fluid, and premonitory variations of ts/tp travel times. *Bulletin of the Seismological Society of America*, *62*, 1217–1222.

Nur, A., & Booker, J. R. (1972). Aftershocks caused by pore fluid flow? *Science*, *175*(4024), 885–887. https://doi.org/10.1126/science.175.4024.8

O'Connell, R. J., & Budiansky, B. (1974). Seismic velocities in dry and saturated cracked solids. *Journal of Geophysical Research*, *79*, 5412–5426. https://doi.org/10.1029/JB079i035p05412

Patanè, D., Barberi, G., Cocina, O., De Gori, P., & Chiarabba, C. (2006). Time-resolved seismic tomography detects magma intrusions at Mount Etna. *Science*, *313*(5788), 821–823. https://doi.org/10.1126/science.1127724

Pezzo, G., Merryman Boncori, J. P., Tolomei, C., Salvi, S., Atzori, S., Antonioli, A., … Giuliani, R. (2013). Coseismic deformation and source modeling of the May 2012 Emilia (northern Italy) earthquakes. *Seismological Research Letters*, *84*(4), 645–655. https://doi.org/10.1785/0220120171

Rovida, A., Camassi, R., Gasperini, P., & Stucchi, M. (2011). *CPTI11, the 2011 version of the parametric catalogue of Italian earthquakes*. Bologna. Retrieved from http://emidius.mi.ingv.it/CPTI(2011: Milano. https://doi.org/10.6092/INGV.IT-CPTI11

Scrocca, D., Carminati, E., Doglioni, C., & Marcantoni, D. (2007). Slab retreat and active shortening along the central-northern Apennines. In O. Lacombe & F. Roure (Eds.), *Thrust belts and foreland basins: From fold kinematics to hydrocarbon system* (pp. 471–487). Berlin, Heidelberg: Springer. https://doi.org/10.1007/978-3-540-69426-7_25

Serpelloni, E., Anderlini, L., Avallone, A., Cannelli, V., Cavaliere, A., Cheloni, D., … Sepe, V. (2012). GPS observations of coseismic deformation following the May 20th and 29, 2012, Emilia seismic events (northern Italy): Data, analysis and preliminary models. *Annales Geophysicae*, *55*(4), 759–766. https://doi.org/10.4401/ag-6168

Sibson, R. H. (2009). Rupturing in overpressured crust during compressional inversion—The case from NE Honshu, Japan. *Tectonophysics*, *473*(3-4), 404–416. https://doi.org/10.1016/j.tecto.2009.03.016

Styles, P., Gasparini, P., Huenges, E., Scandone, P., Lasocki, S., & Terlizzese, F. (2014). *Report on the hydrocarbon exploration and seismicity in Emilia region, International Commission on Hydrocarbon Exploration and Seismicity in the Emilia Region (ICHESE) February* (pp. 1–213). Bologna: Regione Emilia Romagna.

Thurber, C. H. (1983). Earthquake locations and three-dimensional crustal structure in the Coyote Lake area, central California. *Journal of Geophysical Research*, *88*, 8226–8236. https://doi.org/10.1029/JB088iB10p08226

Tizzani, P., Castaldo, R., Solaro, G., Pepe, S., Bonano, M., Casu, F., … Sansosti, E. (2013). New insights into the 2012 Emilia (Italy) seismic sequence through advanced numerical modeling of ground deformation InSAR measurements. *Geophysical Research Letters*, *40*, 1971–1977. https://doi.org/10.1002/grl.50290

Toda, S., Stein, R. S., & Sagiya, T. (2002). Evidence from the AD 2000 Izu islands earthquake swarm that stressing rate governs seismicity. *Nature*, *419*, 58–61. https://doi.org/10.1038/nature00997

Toomey, D. R., & Foulger, G. R. (1989). Tomographic inversion of local earthquake data from the Hengill-Grensdalur central volcano complex, Iceland. *Journal of Geophysical Research*, *94*, 17,497–17,510. https://doi.org/10.1029/JB094iB12p17497

Trippetta, F., Collettini, C., Vinciguerra, S., & Meredith, P. G. (2010). Laboratory measurements of the physical properties of Triassic evaporites from central Italy and correlation with geophysical data. *Tectonophysics*, *492*(1-4), 121–132. https://doi.org/10.1016/j.tecto.2010.06.001

Volpe, M., & Piersanti, A. (2016). The role of fluid migration and static stress transfer in searching connections between the May 2012 Emilia earthquakes through a fully 3D finite element modeling. *Modeling Earth Systems Environment*, *2*(1), 1–12. https://doi.org/10.1007/s40808-016-0087-9

Wadati, K. (1933). On the travel time of earthquake waves (part II). *Geophysical Magazine*, *7*, 101–111.

Wang, Z. (1997). Seismic properties of carbonate rocks. In I. Palaz & K. J. Marfurt (Eds.), *Carbonate seismology*, *Geophysical Developments Series*, (Vol. 6, pp. 29–52). Tulsa, OK: SEG Books. https://doi.org/10.1190/1.9781560802099.ch3